NUMERICAL SIMULATION OF FAST-MODE MAGNETOSONIC WAVES EXCITED BY PLASMOID EJECTIONS IN THE SOLAR CORONA

Liping Yang[1,2], Lei Zhang[1], Jiansen He[1], Hardi Peter[3], Chuanyi Tu[1],
Linghua Wang[1], Shaohua Zhang[4], and Xueshang Feng[2]

[1] School of Earth and Space Sciences, Peking University, 100871 Beijing, China; jshept@gmail.com
[2] SIGMA Weather Group, State Key Laboratory for Space Weather, Center for Space Science and Applied Research,
Chinese Academy of Sciences, 100190 Beijing, China
[3] Max-Planck-Institut für Aeronomie, Max-Planck-Strasse, D-37191 Katlenburg-Lindau, Germany
[4] Center of Spacecraft Assembly Integration and Test, China Academy of Space Technology, Beijing 100094, China
Received 2013 November 25; accepted 2014 December 23; published 2015 February 18

ABSTRACT

The Atmospheric Imaging Assembly instrument on board the *Solar Dynamics Observatory* has directly imaged the fast-propagating magnetosonic waves (FMWs) successively propagating outward along coronal magnetic funnels. In this study we perform a numerical investigation of the excitation of FMWs in the interchange reconnection scenario, with footpoint shearing flow being used to energize the system and drive the reconnection. The modeling results show that as a result of magnetic reconnection, the plasma in the current sheet is heated up by Joule dissipation to ~10 MK and is ejected rapidly, developing the hot outflows. Meanwhile, the current sheet is torn into plasmoids, which are shot quickly both upward and downward. When the plasmoids reach the outflow regions, they impact and collide with the ambient magnetic field there, which consecutively launches FMWs. The FMWs propagate outward divergently away from the impact regions, with a phase speed of the Alfvén speed of ~1000 km s^{-1}. In the $k-\omega$ diagram of the Fourier wave power, the FMWs display a broad frequency distribution with a straight ridge that represents the dispersion relation. With the WKB approximation, at the distance of 15 Mm from the wave source region, we estimate the energy flux of FMWs to be $E \sim 7.0 \times 10^6$ erg cm^{-2} s^{-1}, which is ~50 times smaller than the energy flux related to the tube-channeled reconnection outflow. These simulation results indicate that energetically and dynamically the outflow is far more important than the waves.

Key words: magnetic reconnection – Sun: corona – waves

Supporting material: animations

1. INTRODUCTION

In the past decade, observational analysis and theoretical modeling have shown that the solar atmosphere supports the oscillation or propagation of various modes of magnetohydrodynamic (MHD) waves, such as slow-mode waves (Ofman et al. 1997; De Moortel et al. 2000; Wang et al. 2002, 2009, 2013; Ofman & Wang 2002; Marsh et al. 2003; Ofman & Wang 2008), Alfvén waves (Tomczyk et al. 2007; De Pontieu et al. 2007; Cirtain et al. 2007; Okamoto et al. 2007; Jess et al. 2009; He et al. 2009a, 2009b; McIntosh et al. 2011), and fast-mode waves (Schrijver et al. 1999; Williams et al. 2001, 2002; Nakariakov et al. 2003; McLaughlin et al. 2009). However, as a result of instrumental limitations, fast-propagating magnetosonic waves (FMWs) were scarcely observed in the past. To detect the fast magnetosonic waves, the field of view (FOV) of the instrument should be comparable to the wavelengths of the waves, which are the characteristic size of magnetic structures (e.g., length of coronal loops), and the cadences should be shorter than the typical periods of the waves, which range from a few seconds to several minutes (Nakariakov & Verwichte 2005).

On board the *Solar Dynamics Observatory* (*SDO*), the new Atmospheric Imaging Assembly (AIA) has a $41' \times 41'$ full-Sun FOV at $1''\!.5$ resolution and high cadences up to 10 s, which are all in favor of detecting fast propagating features. Using its EUV observations, Liu et al. (2010) firstly noted the FMWs in the low corona. As a first detailed analysis, Liu et al. (2011) found that the FMWs are driven quasi-periodically at the base of the flaring region and propagate outward along open funnels with a phase speed of up to ~2200 km s^{-1}. They also found that the main

period of the FMWs coincides with quasi-periodic pulsations of the flare, suggesting a common origin of these phenomena. In greater detail, Shen & Liu (2012) investigated an FMW event occurring on 2011 May 30, and they further demonstrated the common physical origin of the FMWs and the accompanying pulsation flare, which is possibly driven by quasi-periodic magnetic reconnection generated by several physical situations, such as the repeated generation of plasmoids, as well as their coalescence. By reanalyzing this event with radio observations, Yuan et al. (2013) found that the FMW pattern is comprised of distinct wave trains with varying periods and wavelengths, and revealed again that the generation of FMWs should be tightly related to energy release in magnetic reconnections. Recently, Shen et al. (2013) presented observations of an FMW in multiple wavelengths and its interaction with other magnetic structures.

So far, great modeling efforts have been devoted to understanding the physics of FMWs in the solar magnetoatmospheres (Cargill et al. 1997; Wu et al. 2001; Bo et al. 2002; Nakariakov et al. 2003; Bogdan et al. 2003; Hasan et al. 2005; Khomenko & Collados 2006; Hasan & van Ballegooijen 2008; Schmidt & Ofman 2010; Fedun et al. 2011; Ofman et al. 2011; Vigeesh et al. 2012; Pascoe et al. 2013). To investigate slow and fast magnetoacoustic-gravity monochromatic wave propagation, transformation, and interaction in the solar photosphere and chromosphere, Bogdan et al. (2003) presented two-dimensional (2D), isothermal MHD simulations with the magnetic configuration consisting of a large unipolar magnetic flux concentration surrounded on each side by two smaller concentrations of opposite-polarity field. To study the processes taking place around the magnetic canopy in a sunspot-like

structure, Khomenko & Collados (2006) conducted similar numerical simulations of magnetoacoustic wave propagation from the photosphere to the low chromosphere. With a global three-dimensional (3D) MHD code, Schmidt & Ofman (2010) simulated a coronal mass ejection of Gibson & Low flux rope type (Gibson & Low 1998) to excite a global FMW. According to the observation results presented by Liu et al. (2011), Ofman et al. (2011) performed a 3D numerical simulation to study the FMW generation, propagation, and trapping in the dipole magnetic field and gravitationally stratified density at coronal temperature. Pascoe et al. (2013) also performed 2D numerical simulations of impulsively generated fast magnetoacoustic perturbations to explore the dispersion of fast magnetoacoustic waves in waveguides. These simulations either used the imposed motions at the bottom boundary as an exciter to study the propagation of the FMWs, or used the large-scale perturbation to study the global nature of the FMWs.

However, recent observations from the AIA indicate that the FMWs may originate from magnetic reconnections associated with the flare (Liu et al. 2011, 2012; Shen & Liu 2012; Yuan et al. 2013). This work aims to provide a numerical investigation of this scenario. Utilizing the developed MHD model (Yang et al. 2013a, 2013b), we simulate the interchange flare scenario with the footpoint shearing flow to energize the system and drive the reconnection. The simulation results show that the plasmoid ejections from the X-point could provoke the FMWs propagating outward. By a comprehensive analysis of these, we find that the modeled FMWs share many features with the observed ones.

2. NUMERICAL MHD MODEL

The details of the 2.5 dimensional (2.5D) numerical MHD model used here have been described in Yang et al. (2013a, 2013b). In brief, the model solves the conservation of mass, momentum, and energy, together with the induction equation. In the energy equation we account for ohmic heating with a switch-on resistivity of the same form as in Yang et al. (2013a). We also synthesize the coronal emission from the model as it would be observed with AIA/*SDO* using the temperature response function (Boerner et al. 2012), following the procedure of Peter & Bingert (2012).

The simulation region spans $0 \, \mathrm{Mm} \leqslant x \leqslant 80 \, \mathrm{Mm}$ in the horizontal dimension and $0 \, \mathrm{Mm} \leqslant y \leqslant 75 \, \mathrm{Mm}$ in the vertical dimension. Initially, the domain is covered by a nonuniform grid in both the x and y dimensions. The grid spacing is $\delta x = \delta y = 25 \, \mathrm{km}$ for $0 \, \mathrm{Mm} \leqslant y \leqslant 4 \, \mathrm{Mm}$, $\delta x = \delta y = 50 \, \mathrm{km}$ for $4 \, \mathrm{Mm} \leqslant y \leqslant 6 \, \mathrm{Mm}$, and $\delta x = \delta y = 100 \, \mathrm{km}$ for $y \geqslant 6 \, \mathrm{Mm}$. During the computation, the smallest grid cells are set in the region with the strongest current, with $\delta x = \delta y = 12.5 \, \mathrm{km}$ as a result of adaptive mesh refinement used in the numerical model. To solve the equations, we use a splitting-based finite-volume numerical scheme. The fluid part is solved by the second-order Godunov-type central scheme and the magnetic part by the constrained transport approach. The explicit second-order total variation diminishing Runge–Kutta time stepping is applied in time integration. Details about the numerics can be found in Feng et al. (2011) and Zhang et al. (2011).

For the initial conditions, the temperature is set as a hyperbolic tangent function as follows:

$$T(y) = T_{\mathrm{chr}} + \frac{1}{2}(T_{\mathrm{cor}} - T_{\mathrm{chr}})\left[\tanh\left(\frac{y - y_{\mathrm{cor}}}{w_{tr}}\right) + 1\right], \quad (1)$$

where T_{cor} and T_{chr} are the respective temperatures in the corona and chromosphere. We set $T_{\mathrm{cor}} = 1 \times 10^6 \, \mathrm{K}$, $T_{\mathrm{chr}} = 2 \times 10^4 \, \mathrm{K}$, $w_{tr} = 1.5 \, \mathrm{Mm}$, and $y_{\mathrm{cor}} = 3.0 \, \mathrm{Mm}$. On the basis of the given function of temperature $T(y)$, the distributions of the pressure $p(y)$ and density $\rho(y)$ are calculated from hydrostatic equilibrium and the ideal gas equation (Yang et al. 2013a, 2013b). The initial velocity is 0. The initial magnetic field is constructed via the vector potential for a uniform background field and an infinite series of line dipoles as described by Edmondson et al. (2010) and used by Lynch & Edmondson (2013). For the boundary conditions, we use the same form as defined by Yang et al. (2013b), except for the footpoint shearing flow to energize the system. At the lower boundary of $y = 0 \, \mathrm{Mm}$, V_z is set to

$$V_z = \begin{cases} 0, & |(x - x_0)| \geqslant d \\ 1.5 \sin(\pi(x - x_0)/d)((x - x_0)^2 - d^2)^2, & |(x - x_0)| \leqslant d, \end{cases}$$
$$(2)$$

where $x_0 = 27 \, \mathrm{Mm}$ and $d = 15 \, \mathrm{Mm}$. The maximum magnitude of the shear flows is $(V_z)_{\mathrm{max}} = 15 \, \mathrm{km \, s^{-1}}$. We note that this value is close to the one employed by Antiochos et al. (1999) and smaller than the one used by Lynch & Edmondson (2013).
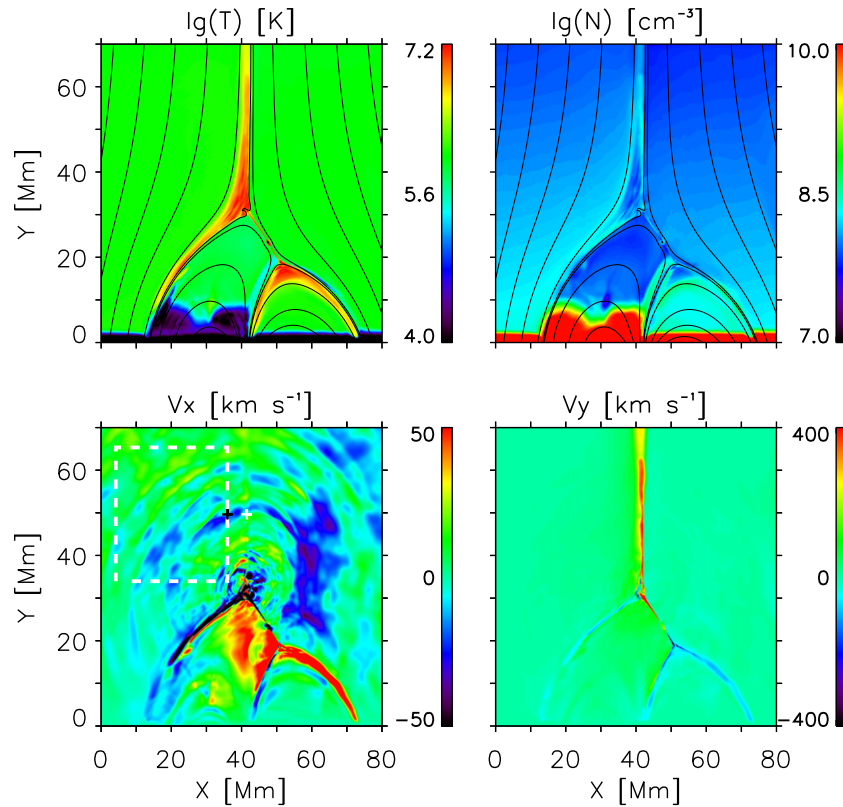
3. NUMERICAL RESULTS

3.1. Outflow from the Reconnection Site

Figure 1 shows the resulting distributions of temperature T, number density N, horizontal velocity V_x (see Animation 1), and vertical velocity V_y (see Animation 2) for a snapshot at $t = 7.13$ minutes. From the figure, we can see that the shearing of the loop causes its field lines to bulge outward, compressing and deforming the null point. The shearing is in the z-direction, i.e., perpendicular to the plane shown in Figure 1. As a result, free magnetic energy and magnetic helicity are injected into the initial current-free system, and electric currents develop along the topological features, such as the null point and within the sheared loop. As the simulation progresses, the shearing motion elongates and strengthens the null-point current sheet, and magnetic reconnection with the creation of plasmoids due to tearing instability takes place. Then, the initially closed sheared-loop field lines open. Meanwhile, the initially open lines close down. Owing to Joule dissipation, the plasma near the null point is heated up to ∼10 MK and is ejected to both sides of the null point, developing a pair of hot outflows, with one shooting upward and the other downward.

From the distribution of the horizontal velocity V_x, as well as Animation 1 and Animation 2 available in the online version of the journal, it can be seen that multiple arc-shaped wave trains are consecutively and alternately launched from the simulated flare. The waves propagate radically outward in nearly circular fronts and finally diminish in amplitude and leave the computation domain successively. It should be noted that this phenomenon has been shown, directly or indirectly, in some studies involving a vertical current sheet (Bárta et al. 2008; Karpen et al. 2012), although those authors did not mention such waves explicitly. The distribution of the vertical velocity V_y and the corresponding Animation 2 show that the slow waves also emanate from the reconnection site, just as in our simulation of a chromospheric jet (Yang et al. 2013b).

3.2. Waves Launched from the Reconnection Site

Figure 2 shows running difference images of temperature (top row), synthesized AIA emission at 171 Å (middle row), and

Figure 1. Calculated distributions of temperature T, number density N, horizontal velocity V_x (see Animation 1), and vertical velocity V_y (see Animation 2) at $t = 7.13$ minutes, where streamlines show the magnetic field lines. The white dashed box indicates the selected region for running difference image and Fourier analysis.
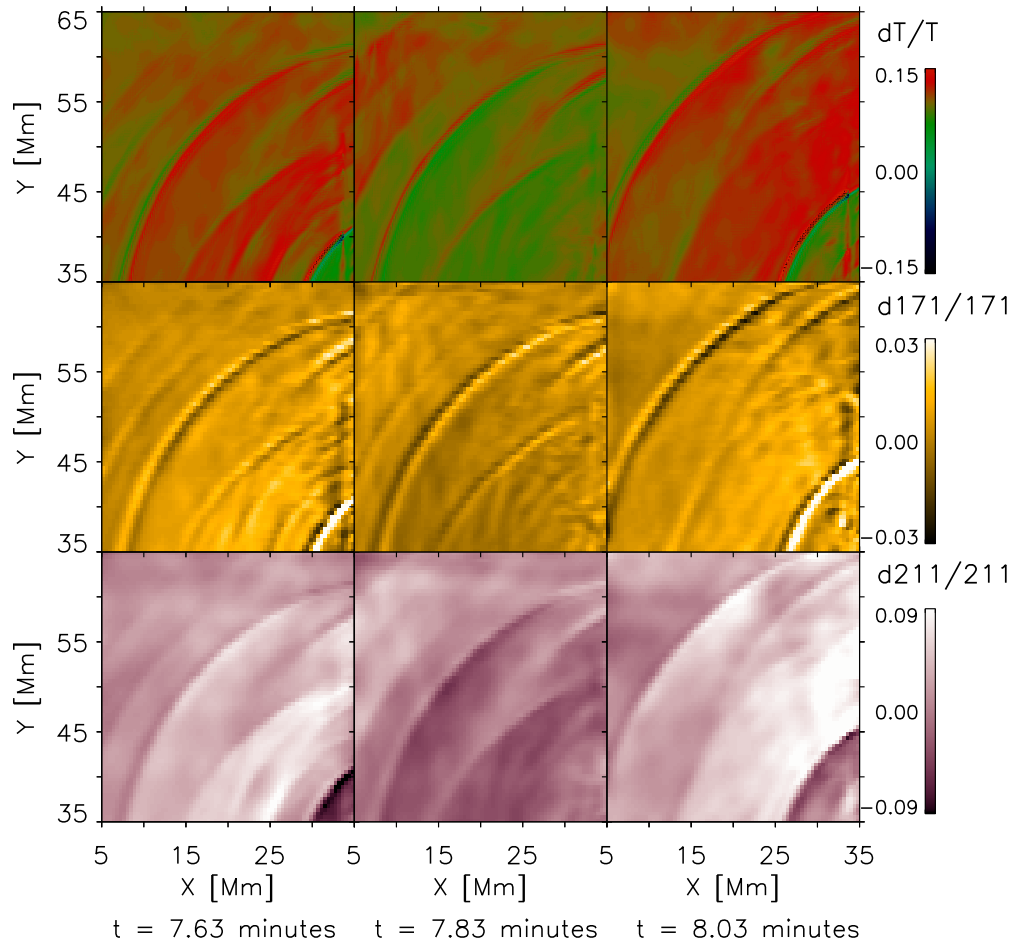
(Animations of this figure are available.)

synthesized AIA emission at 211 Å (bottom row) in the white dashed box region outlined in Figure 1, which is at $t = 7.63$, 7.83, and 8.03 minutes, respectively. To obtain the images at 171 Å and 211 Å, we apply a point-spread function (Gaussian with 1''.4 FWHM) to the synthesized images (0''.6), rebind the images to the AIA pixel size, and finally plot the time series with the same cadence as AIA would observe. It can be seen that the arc-shaped wavefronts of V_x are also observed in the images of temperature, the synthesized real emission at 171 Å, and the synthesized real emission at 211 Å. At $t = 7.63$ minutes, one arc-shaped train enters the selected region. At $t = 7.83$ minutes, it arrives at the center of view. At $t = 8.03$ minutes, the first arc-shaped train exits the view, and another one comes into view and behaves like the first one.

Figure 3 shows temporal evolution of the perturbed velocity components (x: solid; y: dotted), magnetic field components (same legend), and density at the point ($x = 15$ Mm, $y = 45$ Mm) on the path of the waves. The perturbed components are obtained after background detrending. In our case at this point, the fast wave propagates in the upper-left direction, while the background magnetic field aligns quite closely to the y-axis. Polarity relations of fast MHD waves predict that perturbed quantities dB_x and dV_x are in negative correlation, dB_y and dV_x are also in negative correlation, and the perturbed magnetic field is in positive correlation with the perturbed density (Marsch 1986). For fast MHD waves with plasma beta well below 1 like in the solar corona, the perturbed velocity component perpendicular to the background magnetic field (B_0) is much larger than the parallel component. In our case, at the position of our investigation, it is clear that dV_x (almost parallel to B_0) has obviously stronger amplitude than dV_y (almost perpendicular to B_0).

These features are also presented in Figure 4, and thus it is verified that these arc-shaped wave trains, emanated from the reconnection site, are FMWs.

To illustrate how the simulated FMWs are driven, Figure 4 presents the distributions of current density J_z, vertical velocity V_y, and horizontal velocity V_x (see Animation 3) at $t = 6.20$, 6.35, and 6.50 minutes, which are zoomed into the area around the reconnection region. In this figure, we can see that the collision between the ejected plasmoids and the field in the outflow region yields the FMW wave trains as shown in Figures 1 and 2. At $t = 6.20$ minutes, as a result of tearing instability, one plasmoid appears in the current sheet. Pushed by the reconnection outflow, this plasmoid moves upward along the current sheet with a speed of about 500 km s⁻¹. On its way, the plasmoid expands itself. At $t = 6.35$ minutes, it reaches the outflow region and quickly collides and reconnects with the magnetic fields existing there, rapidly releasing its plasma with high thermal pressure. Meanwhile, velocity perturbations in V_x and V_y appear in the outflow region. Another plasmoid is generated in the current sheet and is ejected downward. At $t = 6.50$ minutes, the velocity perturbations evolve into the outward-propagating arc-shaped wave trains, whose wavefronts could be fitted with an arc of a circle with its center at the site of the outflow region. At the same time, the downward-moving plasmoid collides and reconnects with the magnetic field existing at the outflow region, producing the arc-shaped wave trains, which propagate along and across the closed loops. When other plasmoids come into the outflow region, the process mentioned above will be repeated. Animation 3 illustrates that the wave pulses are generated once a plasmoid collides with the outflow region. When traveling outward, the wave pulses

Figure 2. Running difference images of temperature (top row), synthesized real emission at 171 Å (middle row), and synthesized real emission at 211 Å (bottom row) in the white dashed box region shown in Figure 1, which is at $t = 7.63$, 7.83, and 8.03 minutes, respectively.

evolve into distinguishable wavefronts and form multiple wave trains. It is also seen that the wave trains disappear after the coalescence into the outflow region.

To see whether the eigenmode oscillations exist in the loops or not, we plot in Figure 5 the temporal profiles of V_{proj} (the velocity projected onto the slice) at different locations along the loops, with each plot showing the temporal profile at an equidistant position of 0.7 Mm along the loops. The fluctuations in V_{proj} shown in this figure lack evidence of eigenmode oscillations, i.e., the loop does not oscillate as a whole at fundamental or harmonic frequencies, because no identical frequency and relevant phase difference can be identified from the oscillations at various positions. At this point it is unknown why eigenmode oscillations are absent in our simulation. This might be due to strong local damping or expansion of the 2D closed loop. While the eigenmode oscillation of the closed field lines is absent, flare-like magnetic reconnection is found to release the energy in phase with the wave generation.

Figure 6 shows the calculated distribution of Alfvén speed V_A at $t = 7.13$ minutes, with streamlines representing magnetic field lines. The figure exhibits a rather complicated distribution of Alfvén speed V_A, where the Alfvén speeds vary in a wide range from tens to thousands of kilometers per second. Several strong V_A gradients across the magnetic field can be identified at the separatrices between different magnetic topologies. These gradients are formed self-consistently with the evolution of plasma and the magnetic field, rather than prescribed at the beginning. It can be seen that the waveguides confined by the

boundary with the large V_A gradient do not possess a narrow spatial distribution, but extend over large angles, which is different from the results of the previous MHD simulations such as Ofman et al. (2011) and Pascoe et al. (2013). The existence of broad waveguides to confine waves consequently allows the simulated waves to propagate nearly isotropically with wavefronts in arcs with large central angles, rather than only appearing in narrow funnels with limited angular extents as observed by *SDO*/AIA (Liu et al. 2011; Shen & Liu 2012). This figure also indicates that the wave dispersion may be induced by the inhomogeneity of the Alfvén speed adjacent to the wave source region. As the wavefronts travel farther, they become distinguishable from each other (see Animation 3) while the propagation speed increases, and they finally form the multiple wave trains.

3.3. Energy Transport of the Waves and Outflow

To analyze the kinematics of the FMWs, we extract the values of dV_x/V_{A0}, dV_y/V_{A0}, dT/T_0, and dN/N_0 along the direction of wave propagation defined by the right boundary of the dashed box region shown in Figure 1, and we stack the obtained profiles in time sequence. This gives the time–distance diagrams as displayed in Figure 7, showing the steep, recurrent stripes resulting from the arc-shaped FMW wavefronts. The slopes of these stripes correspond to the propagating speeds of the FMWs. By adopting a linear fit with the points shown as the white cross in this figure, we measure the slope of each stripe
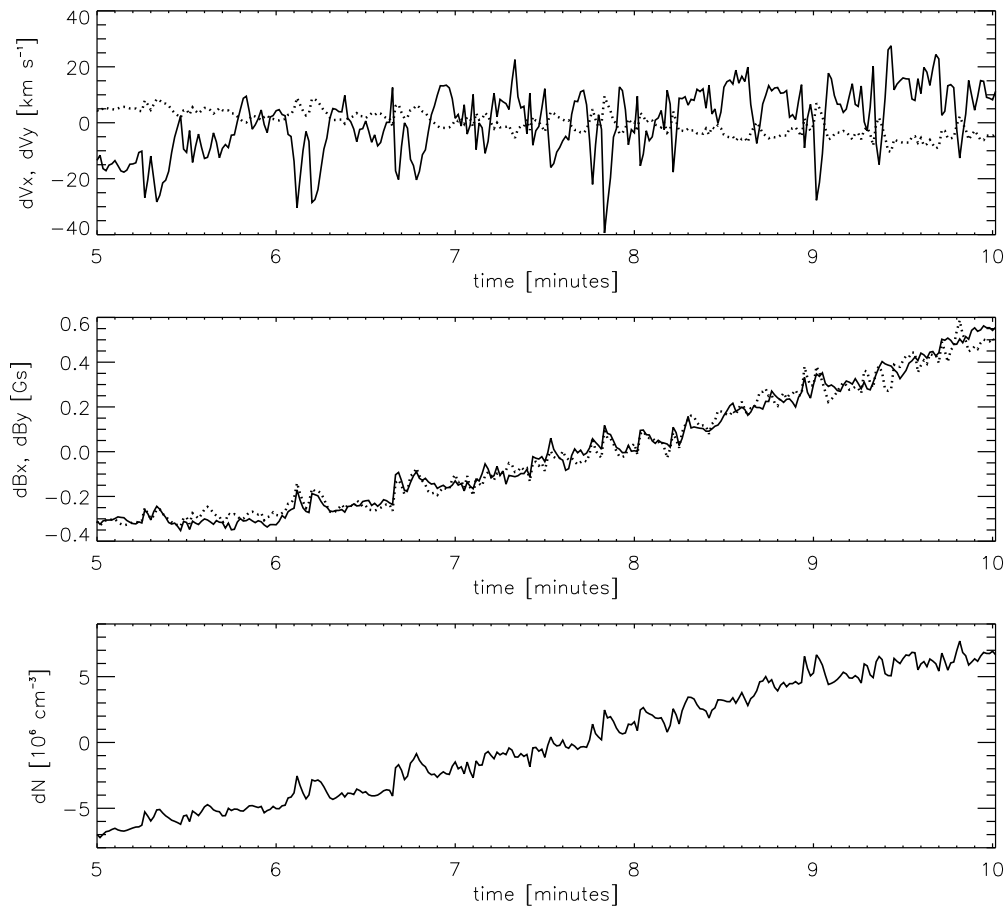
Figure 3. Temporal evolution of the perturbed velocity components (x: solid; y: dotted), magnetic field components (same legend), and density at the point ($x = 15$ Mm, $y = 45$ Mm) on the path of the waves.

and find that the first stripe has a slope of $1057 \pm 25 \, \mathrm{km \, s^{-1}}$, the second a slope of $960 \pm 21 \, \mathrm{km \, s^{-1}}$, and the third a slope of $919 \pm 16 \, \mathrm{km \, s^{-1}}$. This gives an average propagating speed of the wave trains (V_{ph}) of about $1000 \, \mathrm{km \, s^{-1}}$, which is the Alfvén speed in the model. Based on the parameters of these FMWs and the WKB approximation, we can estimate their energy flux by $E = 0.5 \rho (dv)^2 V_{ph}$ (with the nearly equal phase and group velocities seen below). Taking the number density of $10^8 \, \mathrm{cm^{-3}}$ and dv of $30 \, \mathrm{km \, s^{-1}}$ at the distance of $15 \, \mathrm{Mm}$ from the source, marked as the black cross in Figure 1, we obtain a wave energy flux $E \sim 7.0 \times 10^6 \, \mathrm{erg \, cm^{-2} \, s^{-1}}$. This is ~ 50 times smaller than the energy flux related to the tube-confined reconnection outflow at the nearby location marked as the white cross in Figure 1, which has a speed of $\sim 350 \, \mathrm{km \, s^{-1}}$.

Because the FMWs are generated impulsively, their transient nature might be interpreted as propagating wave packets in observations (Liu et al. 2011; Shen & Liu 2012). To investigate the recurrent period behavior of the FMWs, in Figure 8(a) we show a $k-\omega$ diagram of a wave power. Like the analysis of FMW observations, an obvious linear steep ridge that describes the dispersion relation of the FMWs is visible in the simulated $k-\omega$ diagram. This steep ridge can be fitted with a straight line passing through the origin point, which gives average phase ($v_{ph} = \nu/k$) and group ($v_{gr} = d\nu/dk$) velocities of the Alfvén speed of $\sim 1000 \, \mathrm{km \, s^{-1}}$. Figures 8(b)–(d) are the snapshots of the Fourier-filtered Vx images with a narrow Gaussian function centered at the peak frequencies of $0.05 \, \mathrm{s^{-1}}$, $0.15 \, \mathrm{s^{-1}}$, and $0.25 \, \mathrm{s^{-1}}$, respectively. These highlight the corresponding FMW wave trains at different frequencies. Figure 9 plots the

k-averaged power spectrum to frequency, from the distribution displayed in Figure 8. We can see a continuous power spectrum, which basically decreases with increasing frequency without showing evident peaks.

4. SUMMARY AND DISCUSSION

In this study we performed a numerical investigation of the excitation of FMWs in the interchange reconnection in the solar corona. The footpoint-shearing flow is used here to energize the system and drive the reconnection. We find that the FMWs are initiated by plasmoid ejections from the X-point and that the generated FMWs are comparable to the observations.

The modeling results show that the shearing of the loop causes its field lines to bulge outward, compressing and deforming the null point. As a result, the null-point current sheet forms and magnetic reconnection between sheared-loop field lines and open funnel lines takes place, with the creation of plasmoids due to tearing instability. The plasma near the null point is heated up by Joule dissipation to $\sim 10 \, \mathrm{MK}$ and is ejected to both sides of the null point. As a result of the collision between the impacting plasmoids and the field in the outflow region, the multiple arc-shaped fast-mode magnetosonic wave trains are consecutively and alternately launched from the outflow region, quickly propagating outward. Also, there is a one-to-one correlation between the energy release and the wave generation. In contrast, there are no evident eigenmode oscillations in the closed loop, which if they were present could be responsible for the wave excitation.
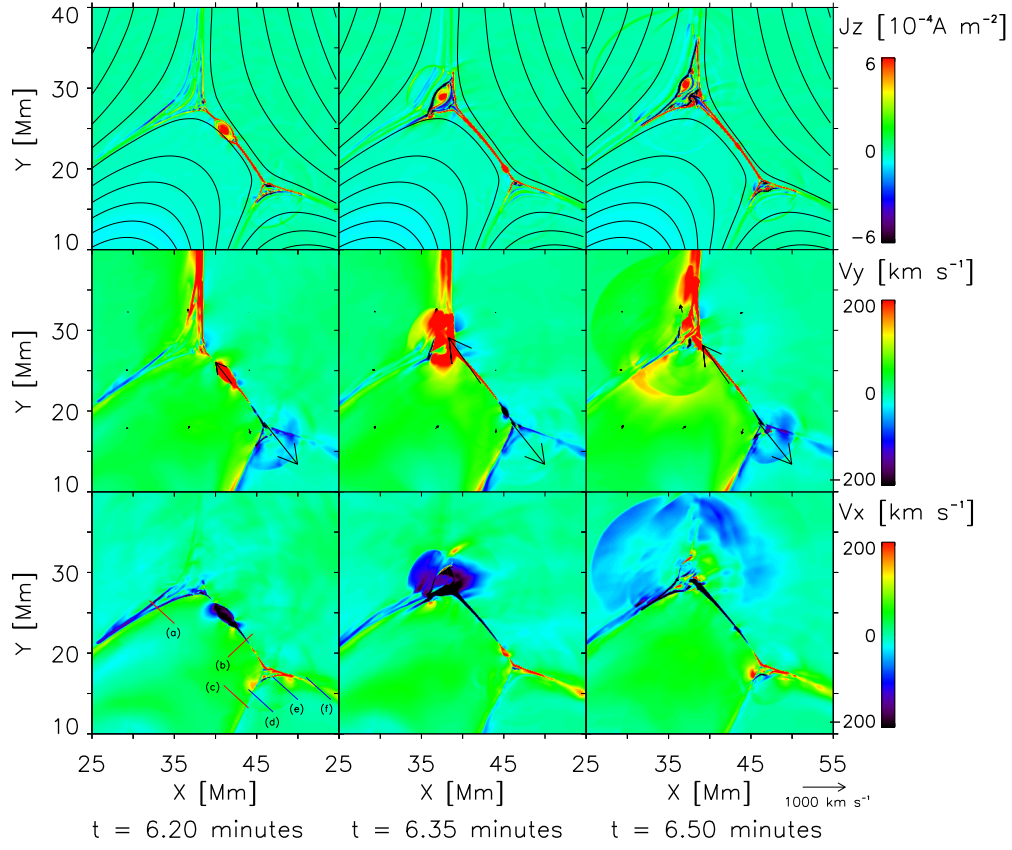
Figure 4. Distributions of current density J_z, vertical velocity V_y, and horizontal velocity V_x at $t = 6.20$, 6.35, and 6.50 minutes, respectively, zoomed into the area around the reconnection region. In this figure, streamlines show magnetic field lines, and black arrows in the middle row denote the velocity.

(An animation of this figure is available.)
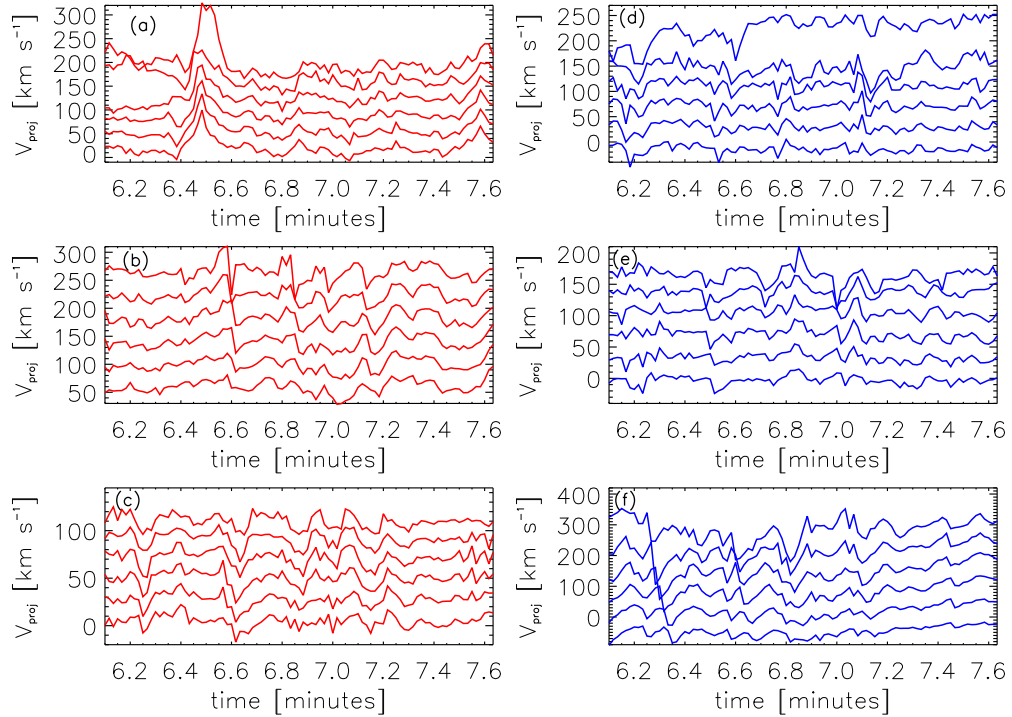
Figure 5. Temporal profiles of V_{proj} (the velocity projected onto the slice) at different locations along the loops. Panels (a)–(f) correspond to slices a–f shown in Figure 4 and Animation 3, respectively. In each panel the horizontal axis represents time, the vertical one V_{proj}; to distinguish the plots, they are stacked with a uniform increment. Each plot shows the temporal profile at an equidistant position of 0.7 Mm along the loops. The lower curves correspond to a position closer to the inside of the loop.
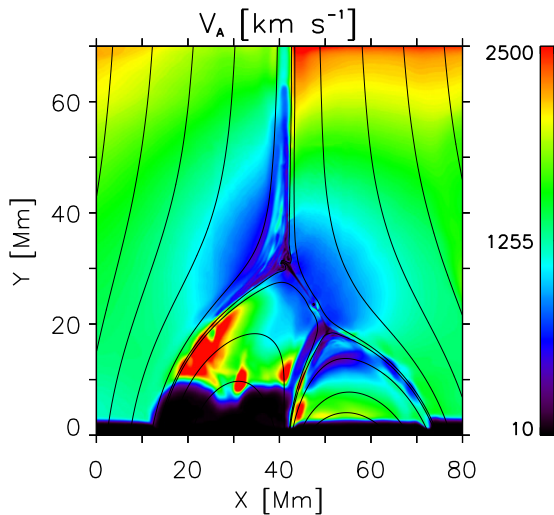
Figure 6. Calculated distribution of Alfvén speed V_A at $t = 7.13$ minutes, where streamlines show the magnetic field lines.

The time–distance diagrams show that the average propagating speed of wave trains (V_{ph}) is about the Alfvén speed of $1000\,\mathrm{km\,s^{-1}}$. For number densities of $10^8\,\mathrm{cm^{-3}}$ and dv of $30\,\mathrm{km\,s^{-1}}$, we found an energy flux of $E \sim 7 \times 10^6\,\mathrm{erg\,cm^{-2}\,s^{-1}}$ with the WKB approximation. This energy flux is $\sim$50 times smaller than the energy flux related to the outflow. The $k-\omega$ diagram of the Fourier wave power shows a broad frequency distribution with a steep ridge that describes the dispersion relation, similar to observations. This steep ridge can be well fitted with a straight line passing through the origin, which gives the

average phase ($v_{ph} = v/k$) and group ($v_{gr} = dv/dk$) velocities of the Alfvén speed of $\sim$1000 km s^{-1}.

In this study, the adopted magnetic geometry is relevant to closed loops reconnecting with open funnels, rather than a vertical current sheet with a Y-type null at one end. Certainly, any geometry involving plasmoid–loop interactions will lead to the generation of fast-mode waves. Our adopted geometry is special and significant in that the generated fast-mode waves propagate not only radically outward along the open funnel but also across the closed loops, which conforms with the observations provided by Shen & Liu (2012). Nevertheless, in the geometry involving a vertical current sheet, the generated waves propagate only laterally and downward, shown indirectly by Bárta et al. (2008) and Karpen et al. (2012). The proximity of our geometry lies in its two Y-type null points, with either one generating its own wave train, and the wave trains may superimpose in some positions and affect the frequency of waves detected there. However, we note that the wave trains produced at the downward Y-type null point are relatively weak, since fewer plasmoids collide at the downward Y-type null point, and even so they are still heavily decelerated while sinking into lower, denser layers (Bárta et al. 2008). We also note that even though a small portion of the wave trains can arrive at the left part of the sheared loops, they are not prone to propagate across it, as Alfvén speeds across this part differ greatly. As a result, the wave trains produced at the lower right Y-type null point may affect just slightly the results of Figure 8. Unfortunately, there are reflected waves from the left-hand side of the sheared loops. The reflected waves are much weaker as compared to the excited waves, so their contribution to the Fourier analysis result in Figure 5 may be negligible. In addition, prior observations and
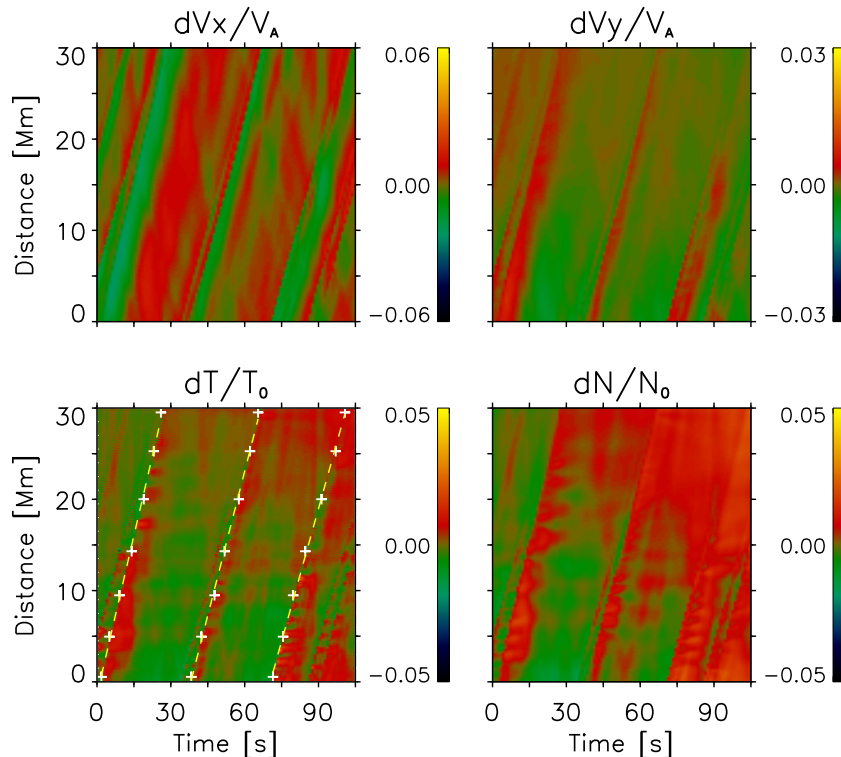
Figure 7. Running difference time–distance diagrams of horizontal velocity dV_x/V_{A0}, vertical velocity dV_y/V_{A0}, temperature dT/T_0, and number density dN/N_0 (for time differences of 1 s). The spatial direction is along the direction of wave propagation defined by the right boundary of the dashed box in Figure 1. V_{A0}, T_0, and N_0 are equal to 1000 km s^{-1}, 10^6 K, and 10^8 cm^{-3}, respectively. The white crosses show the actual points that are used as the linear fits, and the yellow dashed lines indicate the wave propagation speeds.
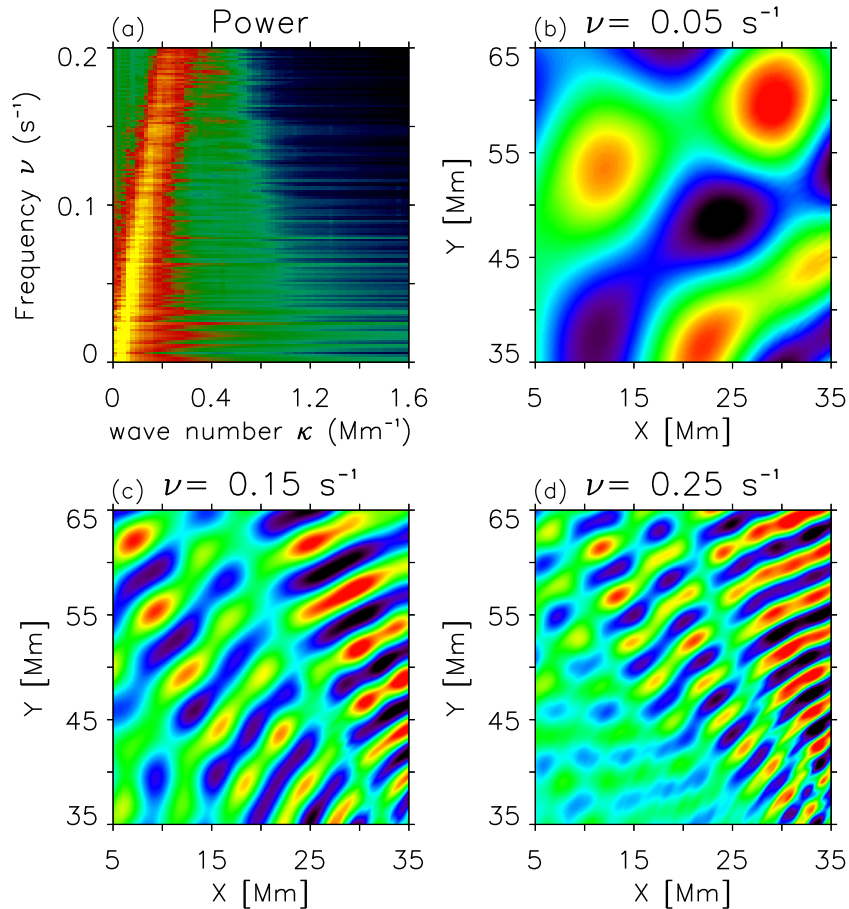
Figure 8. Fourier analysis of FMWs in the dashed-box region shown in Figure 1. (a) Fourier power ($k-\omega$ diagram) of a horizontal velocity field V_x from $t = 6.5$ minutes to $t = 10.0$ minutes. (b)–(d) V_x sample images, which are Fourier-filtered with a narrow Gaussian function centered at the peak frequencies of $0.05\,\text{s}^{-1}$, $0.15\,\text{s}^{-1}$, and $0.25\,\text{s}^{-1}$, respectively.
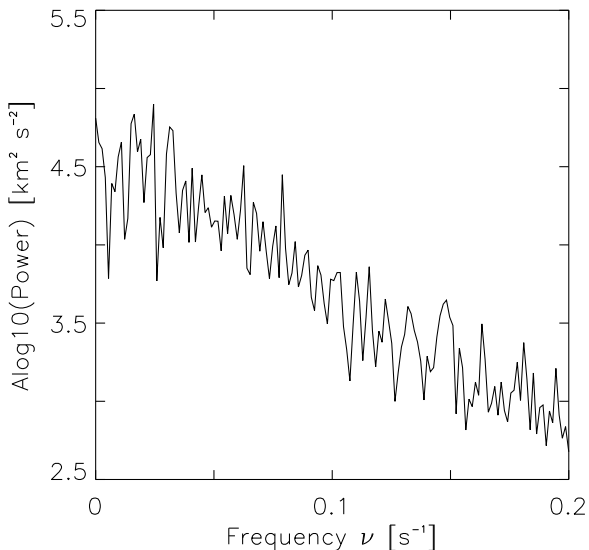
Figure 9. k-averaged power spectrum as a function of frequency, from the distribution displayed in Figure 8.

simulations exhibit evidence of such reflection and bidirectional propagation (Liu et al. 2011; Ofman et al. 2011). The wave contribution from the other Y-type null to the perturbation in the selected region is also negligible in terms of relative fluctuation magnitude.

In this work, we note that the simulated waves propagate isotropically from the source, not appearing in funnels with narrow angular extents as mostly observed by *SDO*/AIA (Liu et al. 2011; Shen & Liu 2012). This difference between the simulated and observed waves may affect their energy, propagation, and even frequencies and presents a possibility for improving our simulations in the future. In addition, we do not reproduce the observed power peaks of the $k-\omega$ ridge. As suggested by Liu et al. (2011) and Shen & Liu (2012), the power peaks may be due to three-minute chromospheric oscillations or the leakage of the pressure-driven p-mode oscillations from the photosphere into the low corona. In the future, we may incorporate these effects to investigate their possible modulation on reconnection and also the excitation of the FMWs. Another issue may arise as a result of the restriction of this work to a 2.5D simulation. Although it is a simple control of the processes at work, the loss of one degree of freedom may affect the energetics of the system and the excision of the FMWs, which has been mentioned in our previous studies (Yang et al. 2013b). Our future works will include an attempt to extend this work to a fully 3D simulation, which will more self-consistently enforce magnetic reconnection between the sheared loop and the ambient fields.

REFERENCES

Antiochos, S. K., DeVore, C. R., & Klimchuk, J. A. 1999, ApJ, 510, 485
Bárta, M., Vršnak, B., & Karlický, M. 2008, A&A, 477, 649
Bo, L., Hui-Nan, Z., & Shui, W. 2002, ChPhL, 19, 1639
Boerner, P., Edwards, C., Lemen, J., et al. 2012, SoPh, 275, 41
Bogdan, T. J., Carlsson, M., Hansteen, V. H., et al. 2003, ApJ, 599, 626
Cargill, P. J., Spicer, D. S., & Zalesak, S. T. 1997, ApJ, 488, 854
Cirtain, J. W., Golub, L., Lundquist, L., et al. 2007, Sci, 318, 1580
De Moortel, I., Ireland, J., & Walsh, R. W. 2000, A&A, 355, L23
De Pontieu, B., McIntosh, S. W., Carlsson, M., et al. 2007, Sci, 318, 1574
Edmondson, J. K., Antiochos, S. K., DeVore, C. R., & Zurbuchen, T. H. 2010, ApJ, 718, 72
Fedun, V., Shelyag, S., & Erdélyi, R. 2011, ApJ, 727, 17
Feng, X., Zhang, S., Xiang, C., et al. 2011, ApJ, 734, 50
Gibson, S. E., & Low, B. C. 1998, ApJ, 493, 460
Hasan, S. S., & van Ballegooijen, A. A. 2008, ApJ, 680, 1542
Hasan, S. S., van Ballegooijen, A. A., Kalkofen, W., & Steiner, O. 2005, ApJ, 631, 1270
He, J., Marsch, E., Tu, C., & Tian, H. 2009a, ApJL, 705, L217
He, J.-S., Tu, C.-Y., Marsch, E., et al. 2009b, A&A, 497, 525
Jess, D. B., Mathioudakis, M., Erdélyi, R., et al. 2009, Sci, 323, 1582
Karpen, J. T., Antiochos, S. K., & DeVore, C. R. 2012, ApJ, 760, 81
Khomenko, E., & Collados, M. 2006, ApJ, 653, 739
Liu, W., Nitta, N. V., Schrijver, C. J., Title, A. M., & Tarbell, T. D. 2010, ApJL, 723, L53
Liu, W., Ofman, L., Nitta, N. V., et al. 2012, ApJ, 753, 52
Liu, W., Title, A. M., Zhao, J., et al. 2011, ApJL, 736, L13
Lynch, B. J., & Edmondson, J. K. 2013, ApJ, 764, 87
Marsch, E. 1986, A&A, 164, 77
Marsh, M. S., Walsh, R. W., De Moortel, I., & Ireland, J. 2003, A&A, 404, L37
McIntosh, S. W., de Pontieu, B., Carlsson, M., et al. 2011, Natur, 475, 477
McLaughlin, J. A., De Moortel, I., Hood, A. W., & Brady, C. S. 2009, A&A, 493, 227
Nakariakov, V. M., Melnikov, V. F., & Reznikova, V. E. 2003, A&A, 412, L7
Nakariakov, V. M., & Verwichte, E. 2005, LRSP, 2, 3
Ofman, L., Liu, W., Title, A., & Aschwanden, M. 2011, ApJL, 740, L33
Ofman, L., Romoli, M., Poletto, G., Noci, G., & Kohl, J. L. 1997, ApJL, 491, L111
Ofman, L., & Wang, T. 2002, ApJL, 580, L85
Ofman, L., & Wang, T. J. 2008, A&A, 482, L9
Okamoto, T. J., Tsuneta, S., Berger, T. E., et al. 2007, Sci, 318, 1577
Pascoe, D. J., Nakariakov, V. M., & Kupriyanova, E. G. 2013, A&A, 560, A97
Peter, H., & Bingert, S. 2012, A&A, 548, A1
Schmidt, J. M., & Ofman, L. 2010, ApJ, 713, 1008
Schrijver, C. J., Title, A. M., Berger, T. E., et al. 1999, SoPh, 187, 261
Shen, Y., & Liu, Y. 2012, ApJ, 753, 53
Shen, Y.-D., Liu, Y., Su, J.-T., et al. 2013, SoPh, 288, 585
Tomczyk, S., McIntosh, S. W., Keil, S. L., et al. 2007, Sci, 317, 1192
Vigeesh, G., Fedun, V., Hasan, S. S., & Erdélyi, R. 2012, ApJ, 755, 18
Wang, T., Ofman, L., & Davila, J. M. 2013, ApJL, 775, L23
Wang, T., Solanki, S. K., Curdt, W., Innes, D. E., & Dammasch, I. E. 2002, ApJL, 574, L101
Wang, T. J., Ofman, L., & Davila, J. M. 2009, ApJ, 696, 1448
Williams, D. R., Mathioudakis, M., Gallagher, P. T., et al. 2002, MNRAS, 336, 747
Williams, D. R., Phillips, K. J. H., Rudawy, P., et al. 2001, MNRAS, 326, 428
Wu, S. T., Zheng, H., Wang, S., et al. 2001, JGR, 106, 25089
Yang, L., He, J., Peter, H., et al. 2013a, ApJ, 770, 6
Yang, L., He, J., Peter, H., et al. 2013b, ApJ, 777, 16
Yuan, D., Shen, Y., Liu, Y., et al. 2013, A&A, 554, A144
Zhang, S.-H., Feng, X.-S., Wang, Y., & Yang, L.-P. 2011, ChPhL, 28, 089601